

EXTRAPOLATION OF THE SOLAR CORONAL MAGNETIC FIELD FROM *SDO*/HMI MAGNETOGRAM BY A CESE–MHD–NLFFF CODE

CHAOWEI JIANG (江朝伟)¹, XUESHANG FENG (冯学尚)¹

Accepted for publication in ApJ

ABSTRACT

Due to the absence of direct measurement, the magnetic field in the solar corona is usually extrapolated from the photosphere in numerical way. At the moment, the nonlinear force-free field (NLFFF) model dominates the physical models for field extrapolation in the low corona. Recently we have developed a new NLFFF model with MHD relaxation to reconstruct the coronal magnetic field. This method is based on CESE–MHD model with the conservation-element/solution-element (CESE) spacetime scheme. In this paper, we report the application of the CESE–MHD–NLFFF code to *SDO*/HMI data with magnetograms sampled for two active regions (ARs), NOAA AR 11158 and 11283, both of which were very non-potential, producing X-class flares and eruptions. The raw magnetograms are preprocessed to remove the force and then inputted into the extrapolation code. Qualitative comparison of the results with the *SDO*/AIA images shows that our code can reconstruct magnetic field lines resembling the EUV-observed coronal loops. Most important structures of the active regions are reproduced excellently, like the highly-sheared field lines that suspend filaments in AR 11158 and twisted flux rope which corresponds to a sigmoid in AR 11283. Quantitative assess of the results shows that the force-free constraint is fulfilled very well in the strong-field regions but apparently not that well in the weak-field regions because of data noise and numerical errors in the small currents.

Subject headings: Magnetic fields; Magnetohydrodynamics (MHD); Methods: numerical; Sun: corona

1. INTRODUCTION

Magnetic field extrapolation is an important tool to study the three-dimensional (3D) solar coronal magnetic field, which is still difficult to measure directly (Sakurai 1989; Aly 1989; Amari et al. 1997; McClymont et al. 1997; Wiegelmann 2008; DeRosa et al. 2009). The models being used most popularly for field extrapolation are the potential field model, the linear force-free field model, and the nonlinear force-free field (NLFFF) model. These models are all based on the same assumption that the Lorentz force is self-balancing in the corona, but adopt different simplifications of the current distribution. Among these models, The NLFFF is the most used one for characterizing magnetic field in the low corona, where there is significant and localized electric current, especially in the active regions (ARs).

But, to directly solve the general NLFFF equation

$$(\nabla \times \mathbf{B}) \times \mathbf{B} = \mathbf{0}, \quad \nabla \cdot \mathbf{B} = 0 \quad (1)$$

is really difficult. As is known, the system is nonlinear intrinsically and even the existence and uniqueness of a solution for a given boundary condition are not proved theoretically; solutions have rarely been found in closed analytic form (e.g., Low & Lou 1990) and in most cases people can only resort to numerical method using computer (many numerical codes have been developed in the past decades, e.g., Wu et al. 1990; Roumeliotis 1996; Amari et al. 1999; Wheatland et al. 2000; Yan & Sakurai 2000; Wiegelmann 2004; Valori et al. 2007; Inoue et al. 2011, one may refer to a recent living review by Wiegelmann & Sakurai (2012)).

Moreover the observation can only provide a bottom boundary of data, and even worse, on the photosphere the field is forced significantly by the dense plasma and thus conflicts with the fundamental force-free assumption. Besides the noise in the observation, measurement error and instrumental uncertainty (e.g., the well known 180° ambiguity of the transverse fields) are all rather unfavorable for practical computation. Thus the observed magnetogram usually needs to be preprocessed to remove the force and noise for providing a better input (Wiegelmann et al. 2006). Anyhow, at present one can hardly seek an exact force-free solution with the observation information fully satisfied. The best we can do is to find a good balance between the force-free constraint and deviation from the real observation, i.e., to seek an approximately force-free solution that matches the photospheric field measurements as well as possible.

Recently we have developed a new extrapolation code called CESE–MHD–NLFFF² (Jiang et al. 2011; Jiang & Feng 2012a), which is based on magnetohydrodynamics (MHD) relaxation method and an advanced numerical scheme, the spacetime conservation-element/solution-element (CESE) method, for faster convergence and better accuracy over the available codes. The good performance and high accuracy of the code have been demonstrated through critical comparisons with previous joint studies by Schrijver et al. (2006) and Metcalf et al.

² We initially planned to develop a full MHD model for computing both the static non-potential field and dynamic evolution of ARs (i.e., the CESE–MHD model, Jiang et al. 2011). But we find that the MHD solver is rather slow to construct the static field, although success has been reported in Jiang et al. (2012a). We thus move to develop a NLFFF version of this model for a faster convergence speed, while the full MHD solver is more suitable for simulating transient events like the eruptions.

cwjjiang@spaceweather.ac.cn, fengx@spaceweather.ac.cn

¹ SIGMA Weather Group, State Key Laboratory for Space Weather, Center for Space Science and Applied Research, Chinese Academy of Sciences, Beijing 100190

(2008), in which various NLFFF codes are assessed based on several NLFFF benchmark tests. We have also successfully extended the code to application in spherical geometry and seamless full-sphere extrapolation for the global corona (Jiang et al. 2012b).

In this paper we report the application of the CESE–MHD–NLFFF code to real solar data, i.e., the presently released *SDO*/HMI magnetograms. To deal with the real observation data, we also have developed a new preprocessing method to remove the force in the raw magnetogram (Jiang & Feng 2013). Extra advancements are made to the original code to further enhance the ability of handling the high-resolution but noisy data. Magnetograms of two ARs, AR 11158 and AR 11283 are sampled for our tests of extrapolation. The results are carefully assessed both qualitatively and quantitatively. We show that our code can recover magnetic field lines resembling the plasma loops seen in the *SDO*/AIA images, and reproduce most important structures of the ARs remarkably well like the highly-sheared field lines that suspend filaments in AR 11158 and twisted flux rope that corresponds to a sigmoid in AR 11283.

The remainder of the paper is organized as follows. We first describe briefly the CESE–MHD–NLFFF code along with its improvements in Section 2. The magnetogram from *SDO*/HMI and the preprocessed result of the raw data are given in Section 3. We then present the extrapolation results for these data including both the raw and preprocessed magnetogram in Section 4. Finally, we draw conclusions and give some outlooks for future work in Section 5.

2. THE CESE–MHD–NLFFF CODE

The basic idea of using the MHD relaxation approach to solve the force-free field is to use some kind of fictitious dissipation to drive the MHD system to an equilibrium in which all the forces can be neglected comparing with the Lorentz force while the boundary magnetogram is satisfied. In this way the Lorentz force should be self-balancing and the field can be regarded as the target force-free solution. We solve the magneto-frictional model equations in the magnetic splitting form as

$$\begin{aligned} \frac{\partial \rho \mathbf{v}}{\partial t} &= (\nabla \times \mathbf{B}_1) \times \mathbf{B} - (\nabla \cdot \mathbf{B}_1) \mathbf{B} - \nu \rho \mathbf{v}, \\ \frac{\partial \mathbf{B}_1}{\partial t} &= \nabla \times (\mathbf{v} \times \mathbf{B}) + \nabla (\mu \nabla \cdot \mathbf{B}_1) - \mathbf{v} \nabla \cdot \mathbf{B}_1, \\ \rho &= |\mathbf{B}|^2 + \rho_0, \quad \mathbf{B} = \mathbf{B}_0 + \mathbf{B}_1. \end{aligned} \quad (2)$$

\mathbf{B} is the target force-free field to be solved, \mathbf{B}_0 is the potential field matching the normal component of the magnetogram, and \mathbf{B}_1 is the deviation between \mathbf{B} and \mathbf{B}_0 . ν is the frictional coefficient and μ is the numerical diffusive speed of the magnetic monopole. The value of them are respectively given by $\nu = 1/(5\Delta t)$ and $\mu = 0.4(\Delta x)^2/\Delta t$ in the code, according to the time step Δt and local grid size Δx . Many advantages can be gained by solving such form of above equations (Jiang & Feng 2012a; Jiang et al. 2012b).

The above equation system (2) is solved by our CESE–MHD scheme (Jiang et al. 2010). In principle we can use any available MHD code to solve this set of equations, since it is a subset of the full MHD system. Taking consideration of the computational efficiency and accuracy,

we prefer to utilize modern advanced MHD codes. However, most of the modern MHD codes are based on theory of characteristic decomposition of a hyperbolic system, thus are not suitable for equation (2), which is not a hyperbolic system. The CESE scheme is a new method free of characteristic decomposition and is very suitable for the equation form here. Furthermore, the CESE–MHD code has been extensively used in solar physics, e.g., the data-driven evolution modeling of AR (Jiang et al. 2012a), the global corona (Feng et al. 2012) and the interplanetary solar wind (Feng et al. 2012; Yang et al. 2012).

To adapt for the application to real solar data, we have made extra improvements to the previous version of CESE–MHD–NLFFF. The first improvement is made to enhance the ability of handling noisy data in the magnetograms. In the noisy weak-field regions of magnetograms (where the signal-to-noise ratio is small, say $|\mathbf{B}| \leq 100$ G), the term $(\nabla \times \mathbf{B}) \times \mathbf{B}/|\mathbf{B}|^2$ could be very large due to numerical gradients of the random noise, thus the velocity \mathbf{v} is prone to be accelerated to extremely high, which can severely restrict the time step and slow the relaxation process of the entire system, even making the computation unmanageable. To deal with this difficulty, the pseudo-plasma density ρ is designed with $\rho_0 = B_{\min}^2 \exp(-z/H_m)$, where z is the height from the bottom surface and $B_{\min} = 100$ G, $H_m = 5$ pixel. In this way, the velocity (near the bottom magnetogram) in the weak-field regions can be reduced significantly, while it is barely affected in the strong-field regions.

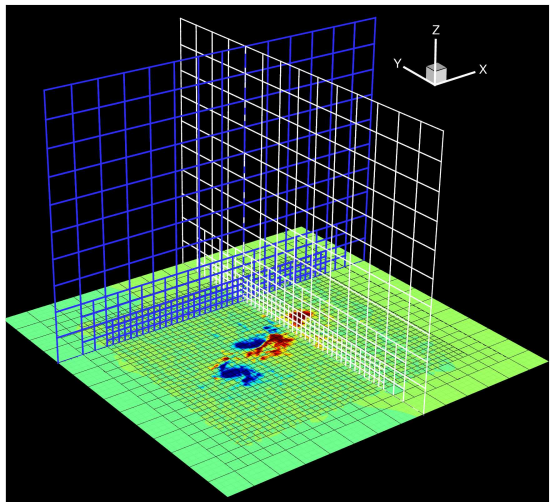


FIG. 1.— The grid structure: the entire volume is divided into blocks and each block has $8 \times 8 \times 8$ cells. Slices through the volume in three axis directions are plotted to show the structure of the blocks and the bottom contour map represents B_z on the photosphere.

Secondly, to deal with the high-resolution observation data, the extrapolation is performed on a non-uniform grid within a block-structured, distributed-memory parallel computational framework (e.g., Jiang et al. 2012a). Specifically, the whole computational volume is divided into blocks with different spatial resolution, and the blocks are evenly distributed among the processors. Within this framework, we have lots of freedom to configure the mesh and save computational resources com-

paring with a uniform grid. As concentrated strongly in the photosphere but expanding rapidly into the corona due to abrupt drop of the gas pressure, the coronal field becomes smoother and weaker successively with height. Naturally we use a grid with decreasing resolution with height: at the bottom the grid spacing matches the resolution of the magnetogram and up to the top of the model box, the grid spacing is increased by, say, four times. At present we use the same resolution in the horizontal plane, and application of adaptive resolution based on the pattern of magnetic flux distribution is under development. With this framework, we also add some coarse buffer blocks around the central volume to reduce influence by the numerical boundaries without adding much computational burden. An example of the grid is shown in Figure 1.

Routinely the quantities in the computational volume is initialized by setting $\mathbf{B}_1 = \mathbf{0}$ and $\mathbf{v} = \mathbf{0}$. The potential field \mathbf{B}_0 is obtained by a Green’s function method (e.g., Metcalf et al. 2008). The bottom boundary is incrementally fed with the observed vector magnetogram in tens of Alfvén time τ_A , while all the other numerical boundaries are fixed with $\mathbf{B}_1 = \mathbf{0}$ and $\mathbf{v} = \mathbf{0}$.

3. DATA

3.1. The HMI Data

The Helioseismic and Magnetic Imager (HMI) on board the *Solar Dynamics Observatory* (*SDO*) provides photospheric vector magnetograms with a high resolution both in space and time. It observes the full Sun with a $4K \times 4K$ CCD whose spatial sampling is 0.5 arcsec per pixel. Raw filtergrams are obtained at 6 different wavelengths and 6 polarization states in the Fe I 6173 Å absorption line, and are collected and converted to observable quantities (like Dopplergrams, continuum filtergrams, and line-of-sight and vector magnetograms) on a rapid time cadence. For the vector magnetic data, each set of filtergrams takes 135 s to be completed. To obtain vector magnetograms, Stokes parameters are first derived from filtergrams observed over a 12-min interval and then inverted through the Very Fast Inversion of the Stokes Vector (Borrero et al. 2011). The 180° azimuthal ambiguity in the transverse field is resolved by an improved version of the “minimum energy” algorithm (Leka et al. 2009). Regions of interest with strong magnetic field are automatically identified near real time (Turmon et al. 2010). A detailed description on how the vector magnetograms are produced can be found on the website // <http://jsoc.stanford.edu/jsocwiki/VectorPaper>.

The magnetogram data we use here is downloaded from <http://jsoc.stanford.edu/jsocwiki/VectorPaper>, where the HMI vector magnetic field data series `hmi.B_720s_e15w1332` are released for several ARs. There are two special formats, i.e., direct cutouts and remapped images. We use the remapped format which is more suitable for modeling in local Cartesian coordinates, since the images are computed with a Lambert cylindrical equal area projection centered on the tracked region. For our test, we select two ARs, AR 11158 and AR 11283, both of which produced X-class flares and were very non-potential. The full resolution of the data is about $0.5''$ per pixel and we rebin them to $1''$ per pixel for the NLFFF modeling.

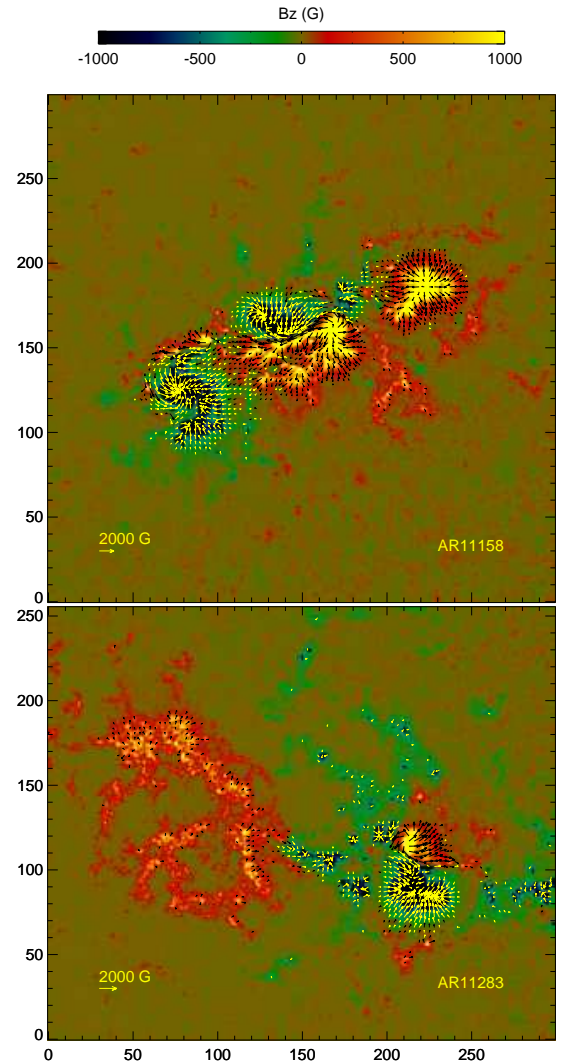


FIG. 2.— Vector magnetograms for AR 11158 and AR 11283. The background shows the vertical components with saturation values of ± 1000 G; the vectors represent the transverse fields (above 200 G). The length unit is arcsec.

AR 11158 is a well-known target studied in many recent works for different purposes (e.g., Schrijver et al. 2011; Sun et al. 2012b; Liu et al. 2012; Jing et al. 2012), and was selected by Wiegmann et al. (2012) for special test on optimizing their extrapolation code with HMI data. This AR has a multipolar and complex structure. It produced several major flares and coronal mass ejections (CMEs) during its disk passage, including the first X-class flare of cycle 24 on 2012 February 15. Figure 2 (the first panel) shows a vector magnetogram of AR 11158 taken at 20:36 UT on 2011 February 14, which will be used for our computation. This AR is well isolated from other ones and is almost flux-balanced (see Table 1), with the main polarities concentrated in the central field of view (FoV). As can be seen, the field shows a strong shearing along the polarity inversion lines (PILs).

Another one, AR 11283, is also very eruptive, generating several X-class flares and CMEs. We select a magnetogram taken at 22:00 UT on September 6, just prior to a major flare at 22:20 UT. The magnetogram is shown in the second panel of Figure 2. As an input for extrapola-

tion, this data is not good as AR 11158's, since the flux is dispersed with some strong polarities almost on the edge of the FoV. Also the total flux is not well balanced (see Table 1), which is unfavorable for our extrapolation.

3.2. Data Preprocessing

Generally, the raw magnetogram cannot be inputted directly into the NLFFF code because the intrinsic non-force-freeness of the photospheric field violates the force-free assumption. According to the derivation by [Molodenskii \(1969\)](#) and [Aly \(1989\)](#), an ideally force-free magnetogram should fulfill the following conditions:

$$\begin{aligned} \int_S B_z dx dy = 0, \quad F_x = \int_S B_x B_z dx dy = 0, \\ F_y = \int_S B_y B_z dx dy = 0, \quad F_z = \int_S E_B dx dy = 0, \\ T_x = \int_S y E_B dx dy = 0, \quad T_y = \int_S x E_B dx dy = 0, \\ T_z = \int_S (y B_x B_z - x B_y B_z) dx dy = 0 \end{aligned} \quad (3)$$

where $E_B = B_x^2 + B_y^2 - B_z^2$. These expressions are derived from the volume integrals of the total divergence, magnetic force and torque of an ideally force-free field

$$\int_V \nabla \cdot \mathbf{B} dV = 0, \quad \int_V \mathbf{j} \times \mathbf{B} dV = \mathbf{0}, \quad \int_V \mathbf{r} \times (\mathbf{j} \times \mathbf{B}) dV = \mathbf{0} \quad (4)$$

(by using Gauss' divergence theorem, the volume integrals 4 can be transformed to the surface integrals 3). In the case of the coronal field, the surface integrals of Equation (3) are usually restricted within the bottom magnetogram since the contribution from other boundaries can be neglected. To assess the real data with respect to the force-free condition, three parameters are usually computed as ([Wiegelmann et al. 2006](#))

$$\begin{aligned} \epsilon_{\text{flux}} = \frac{\int_S B_z dx dy}{\int_S |B_z| dx dy}, \quad \epsilon_{\text{force}} = \frac{|F_x| + |F_y| + |F_z|}{\int_S P_B dx dy}, \\ \epsilon_{\text{torque}} = \frac{|T_x| + |T_y| + |T_z|}{\int_S \sqrt{x^2 + y^2} P_B dx dy} \end{aligned} \quad (5)$$

where $P_B = B_x^2 + B_y^2 + B_z^2$. Small values of these quantities, e.g., $\epsilon_{\text{flux}}, \epsilon_{\text{force}}, \epsilon_{\text{torque}} \ll 1$ indicate a good input for the NLFFF modeling. Table 1 shows that for AR 11158, the force-free condition is satisfied quiet well with flux almost balanced and $\epsilon_{\text{force}}, \epsilon_{\text{torque}}$ less than 0.1; while for AR 11283, it is worse. Note that the flux non-balance will pose a negative effect on the extrapolation (see Section 4).

Besides the non-force-freeness, the observed data contains measurement noise which is also unfavorable for practical implementation of extrapolation. To this end, preprocessing of the raw magnetogram has been proposed by [Wiegelmann et al. \(2006\)](#) to remove the force and noise for providing better input for NLFFF modeling. To be consistent with our extrapolation code using a magnetic splitting form, we recently developed a new code for magnetogram preprocessing ([Jiang & Feng 2013](#)), in which the vector magnetogram is also split into a potential field part and a non-potential field part and

we deal with the two parts separately. Preprocessing of the potential part is simply performed by taking the data sliced at a plane about 400 km above the photosphere³ from the 3D potential field which is extrapolated from the observed vertical field. Then the non-potential part is modified and smoothed by an optimization method to fulfill the constraints of total magnetic force-freeness and torque-freeness, which is similar to the method proposed by [Wiegelmann et al. \(2006\)](#). We have paid particular attention to the extents the force is needed to be removed and the smoothing can be performed. As for practical computation based on numerical discretization, an accurate satisfaction of force-free constraints is apparently not necessary. Also the extent of the smoothing for the data needs to be carefully determined, if we want to mimic the expansion of the magnetic field from the photosphere to some specific height above. We use the values of force-freeness and smoothness calculated from the pre-processed potential-field part as a reference to guide the preprocessing of the non-potential field part, i.e., we require that the target magnetogram has the same level of force-freeness and smoothness as its potential part. These requirements can restrict well the free parameters, i.e., the weighted factors in the optimization function.

The results of preprocessed data are also given in Table 1 together with results of their numerical potential-field part. For both magnetograms, the preprocessing reduces the parameters ϵ_{force} and ϵ_{torque} by more than one order of magnitude, making the residual force around the level of numerical error (i.e., the parameters are close to those of the numerical potential field). The parameters S_x, S_y, S_z in the table measure the smoothness of the components B_m ($m = x, y, z$), which are defined by (see [Jiang & Feng 2013](#))

$$S_m = \sum_p [(\Delta B_m)^2] / \sum_p [(\bar{\Delta} B_m)^2] \quad (6)$$

where the summation \sum_p is over all the pixels of the magnetogram, and Δ is a usual five-point 2D-Laplace operator, i.e., for pixel (i, j)

$$\begin{aligned} \Delta B_{i,j} &\equiv B_{i+1,j} + B_{i-1,j} + B_{i,j+1} + B_{i,j-1} - 4B_{i,j}, \\ \bar{\Delta} B_{i,j} &\equiv B_{i+1,j} + B_{i-1,j} + B_{i,j+1} + B_{i,j-1} + 4B_{i,j}. \end{aligned} \quad (7)$$

As shown the smoothness of the preprocessed data is very close to those of their potential part, and is consistent among three components, which is unlike the raw data with very different smoothness for different components. Smoothing of the data can be clearly seen by comparing the raw and preprocessed magnetograms as shown in Figure 3, and especially in the J_z map which shows the random noise is suppressed effectively (but not totally).

Readers should be reminded that the constraints of Equation (3) are only necessary conditions, but not sufficient for an ideally force-free magnetogram, meaning that the magnetogram may still contains force even these conditions are satisfied. What we can say is that the

³ We choose such height because the field becomes force-free in the chromosphere roughly 400 km above the photosphere according to ([Metcalf et al. 1995](#)). Our preprocessing code is designed to modify the photospheric magnetogram to mimic a force-free chromospheric magnetogram at such height.

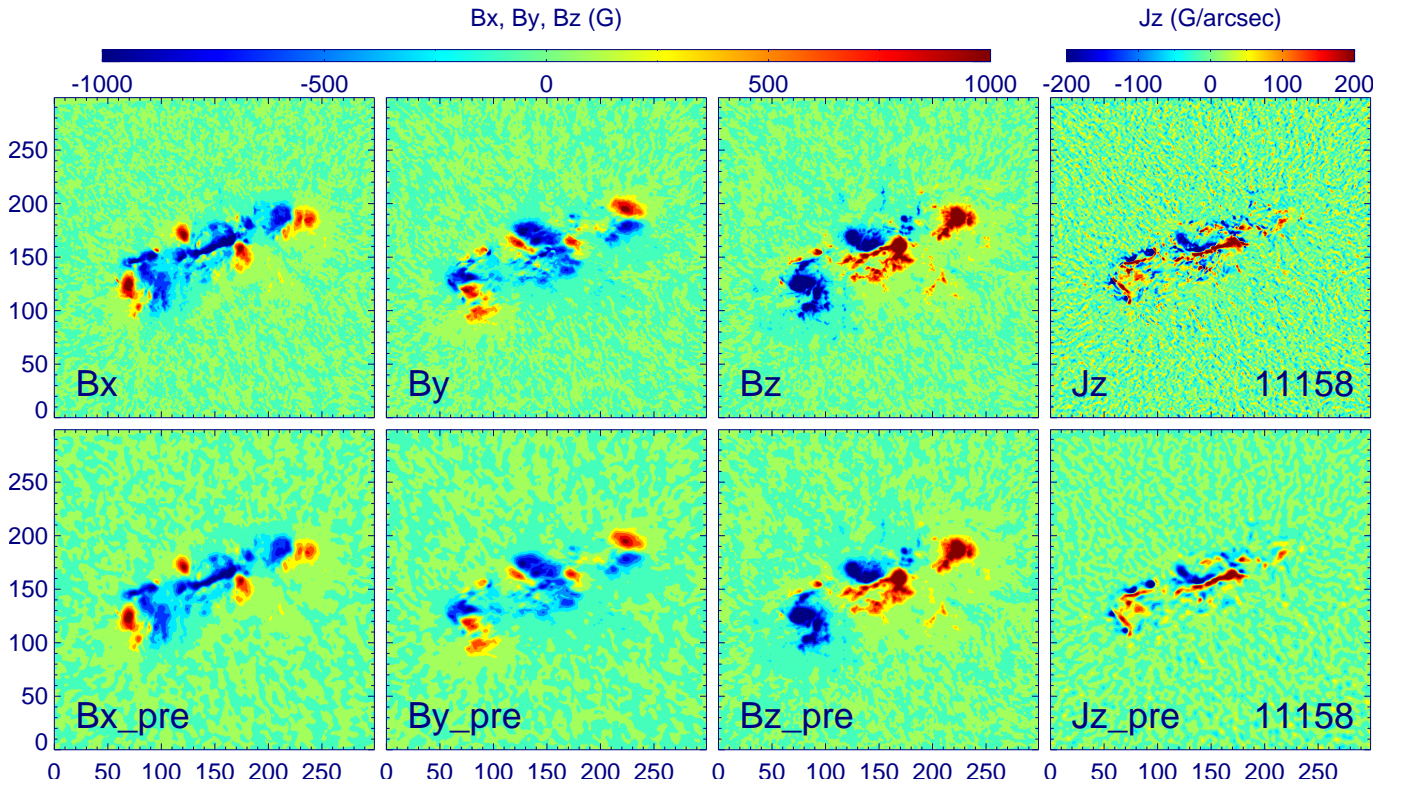


FIG. 3.— Raw and preprocessed magnetograms for AR 11158.

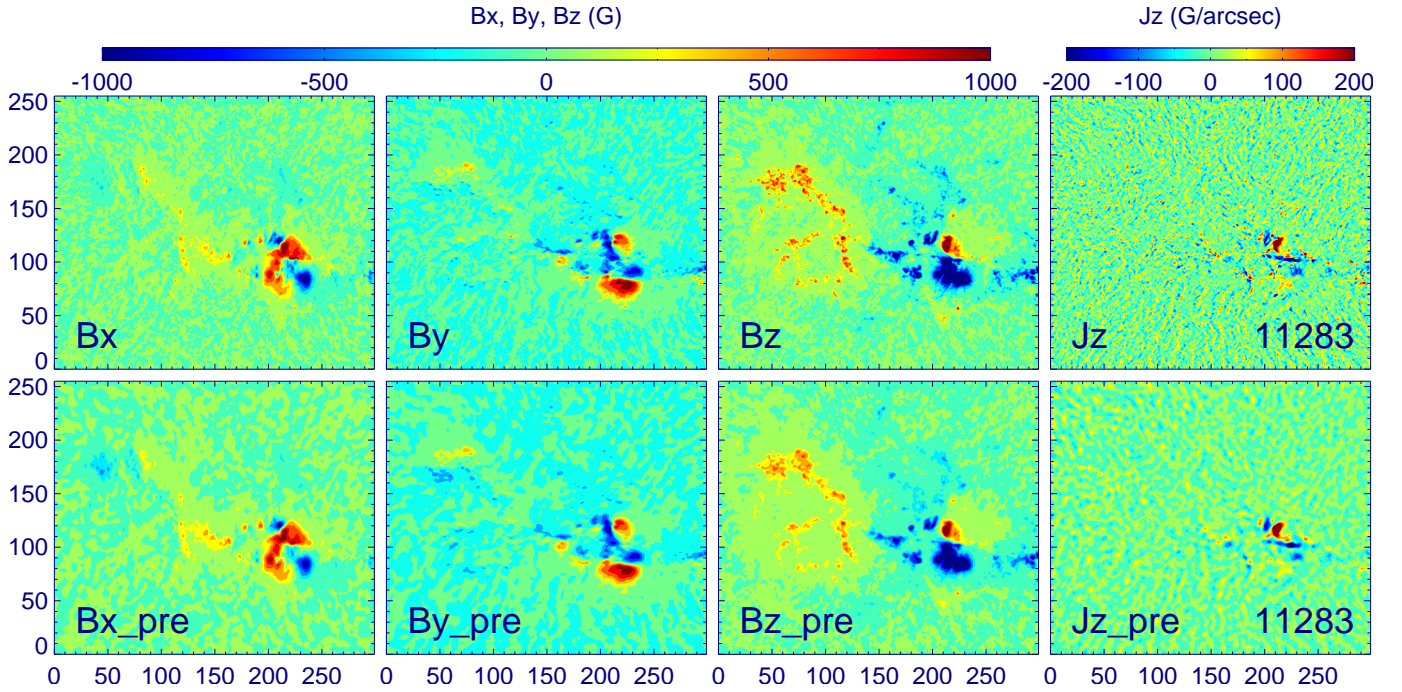


FIG. 4.— Raw and preprocessed magnetograms for AR 11283.

preprocessed magnetogram is more suitable for NLFFF modeling than the raw data, but not a completely consistent boundary condition.

4. RESULTS

4.1. AR 11158

The observed coronal loops in X-ray and EUV images give us a proxy of the magnetic field line geometry and are thus a good constraint for the magnetic field model besides the vector magnetograms (e.g., [Aschwanden et al. 2012](#); [Malamushenko et al. 2012](#)). In Figure 5 we compare the extrapolated field with coronal loops observed by *SDO*/AIA in the wavelength of 171 Å, in which the

| Data | ϵ_{flux} | ϵ_{force} | ϵ_{torque} | S_x | S_y | S_z |
|---------------------|--------------------------|---------------------------|----------------------------|----------|----------|----------|
| AR 11158 | | | | | | |
| Raw map | 0.017 | 0.072 | 0.073 | 5.05E-03 | 6.12E-03 | 1.05E-03 |
| Preprocessed map | 0.019 | 0.002 | 0.002 | 7.83E-05 | 1.01E-04 | 8.74E-05 |
| Numerical potential | 0.019 | 0.001 | 0.002 | 8.78E-05 | 8.42E-05 | 8.74E-05 |
| AR 11283 | | | | | | |
| Raw map | -0.111 | 0.193 | 0.143 | 1.12E-02 | 1.15E-02 | 1.94E-03 |
| Preprocessed map | -0.119 | 0.012 | 0.017 | 1.73E-04 | 1.95E-04 | 1.79E-04 |
| Numerical potential | -0.119 | 0.011 | 0.017 | 1.98E-04 | 1.63E-04 | 1.79E-04 |

TABLE 1
QUALITY OF THE MAGNETOGRAMS.

| Region | CWsin | C ² Wsin | $\langle f_i \rangle$ | E_{tot} | E_{pot} | E_{free} | $E_{\text{free}}/E_{\text{pot}}$ | $E_{\text{free}}/(E_{\text{free}})_{\text{full}}$ |
|--------------|-------|---------------------|-------------------------|------------------|------------------|-------------------|----------------------------------|---|
| Raw | | | | | | | | |
| Full | 0.32 | 0.18 | 6.59E-04 | 10.9 | 8.97 | 1.93 | 22% | 100% |
| A | 0.18 | 0.11 | 1.25E-03 | 8.3 | 6.24 | 2.06 | 33% | 107% |
| B | 0.07 | 0.06 | 7.17E-04 | 3.24 | 2.09 | 1.15 | 55% | 60% |
| C | 0.16 | 0.11 | 1.64E-03 | 0.67 | 0.47 | 0.20 | 43% | 10% |
| Preprocessed | | | | | | | | |
| Full | 0.30 | 0.14 | 6.18E-04 | 9.83 | 8.18 | 1.65 | 20% | 100% |
| A | 0.17 | 0.10 | 1.20E-03 | 7.54 | 5.61 | 1.93 | 34% | 117% |
| B | 0.06 | 0.05 | 7.20E-04 | 2.97 | 1.81 | 1.16 | 64% | 70% |
| C | 0.16 | 0.12 | 1.67E-03 | 0.59 | 0.42 | 0.17 | 40% | 10% |

TABLE 2
RESULTS OF THE METRICS FOR AR 11158. FULL REGION IS EXTRAPOLATION BOX OF $[0, 300](x) \times [0, 300](y) \times [0, 150](z)$. REGION A IS $[53, 222] \times [104, 191] \times [0, 50]$; REGION B IS $[116, 181] \times [145, 175] \times [0, 30]$; REGION C IS $[62, 102] \times [132, 161] \times [0, 20]$. THE FOVS OF THE REGIONS ARE SHOWN BY THE BOXES IN FIGURE 6. THE ENERGY UNIT IS 10^{32} ERG.

loops are visible the best than in other channels. The field lines are traced from the photosphere at locations selected roughly according to the footpoints of the visible bright loops, and are rendered with different colors for a better looking. The view angle of the field lines is aligned with the AIA image. We plot the field lines and the AIA image both alone and overlaid for a better inspecting of the result. As shown from an overview of the images, most of the extrapolated field lines closely resemble the observed loops. At the central region the field lines are strongly sheared along the major PIL and slightly twisted (as compared with the potential solution), indicating the existence of strong electric currents along the field lines. In the left panel of Figure 6, we plot an image of vertical integral of the current density in the extrapolation volume, and the strong-current regions are outlined by the boxes (labeled as A, B and C). Note that the currents are strongly localized within the central region B and a smaller region C. The magnetic structures of the strong-current regions are shown in the right panel of Figure 6. As can be seen, the twist of the field lines in region C is much stronger than that in region B. The results support observation studies which show that a filament related with a X-class flare and CME exists in the core region B (Sun et al. 2012b), and there are small eruptions in region C due to flux emergence (Sun et al. 2012a).

Nevertheless, we note that the misalignments between the modeling field lines and the observation are also obvious, especially, the large loops near the north-west boundary of the FoV. There are several reasons for the misalignments: first, a local Cartesian coordinate system is not adequate to include the large loops which obviously need spherical geometry; second, the FoV of magnetogram may be not large enough to properly char-

acterize the entire relevant current system, which again needs the curvature of the Sun's surface to be taken into account; third, it is not easy to locate precisely the photospheric footpoints of different loops that spread apart distinctly in the corona but are rooted very closely in the photosphere; fourth, the coronal field may be rather dynamic, e.g., expands or oscillates due to eruptions, which makes the static extrapolation fail. We know that this visual comparison between the model result and observation is very preliminary, and more critical comparison is required, for example, with the 3D loops reconstructed with multi-points observation (DeRosa et al. 2009; Aschwanden 2011).

Routinely, we check the quality of the numerical result by computing several metrics. The force-freeness of the extrapolation data is usually measured by a current-weighted sine metric (CWsin) defined by

$$\text{CWsin} \equiv \frac{\int_V J \sigma dV}{\int_V J dV}; \quad \sigma = \frac{\mathbf{J} \times \mathbf{B}}{JB}, \quad (8)$$

where $B = |\mathbf{B}|$, $J = |\mathbf{J}|$ and V is the computational volume. We also compute a current-square-weighted sine metric (C²Wsin) similarly defined by

$$\text{C}^2\text{Wsin} \equiv \frac{\int_V J^2 \sigma dV}{\int_V J^2 dV}, \quad (9)$$

with more weight on the strong-current regions. The divergence-freeness is measured by $\langle |f_i| \rangle$

$$\langle |f_i| \rangle = \frac{1}{V} \int_V \frac{\nabla \cdot \mathbf{B}}{6B/\Delta x} dV. \quad (10)$$

We care about different energy contents, i.e., the total energy E_{tot} , the potential energy E_{pot} and the free en-

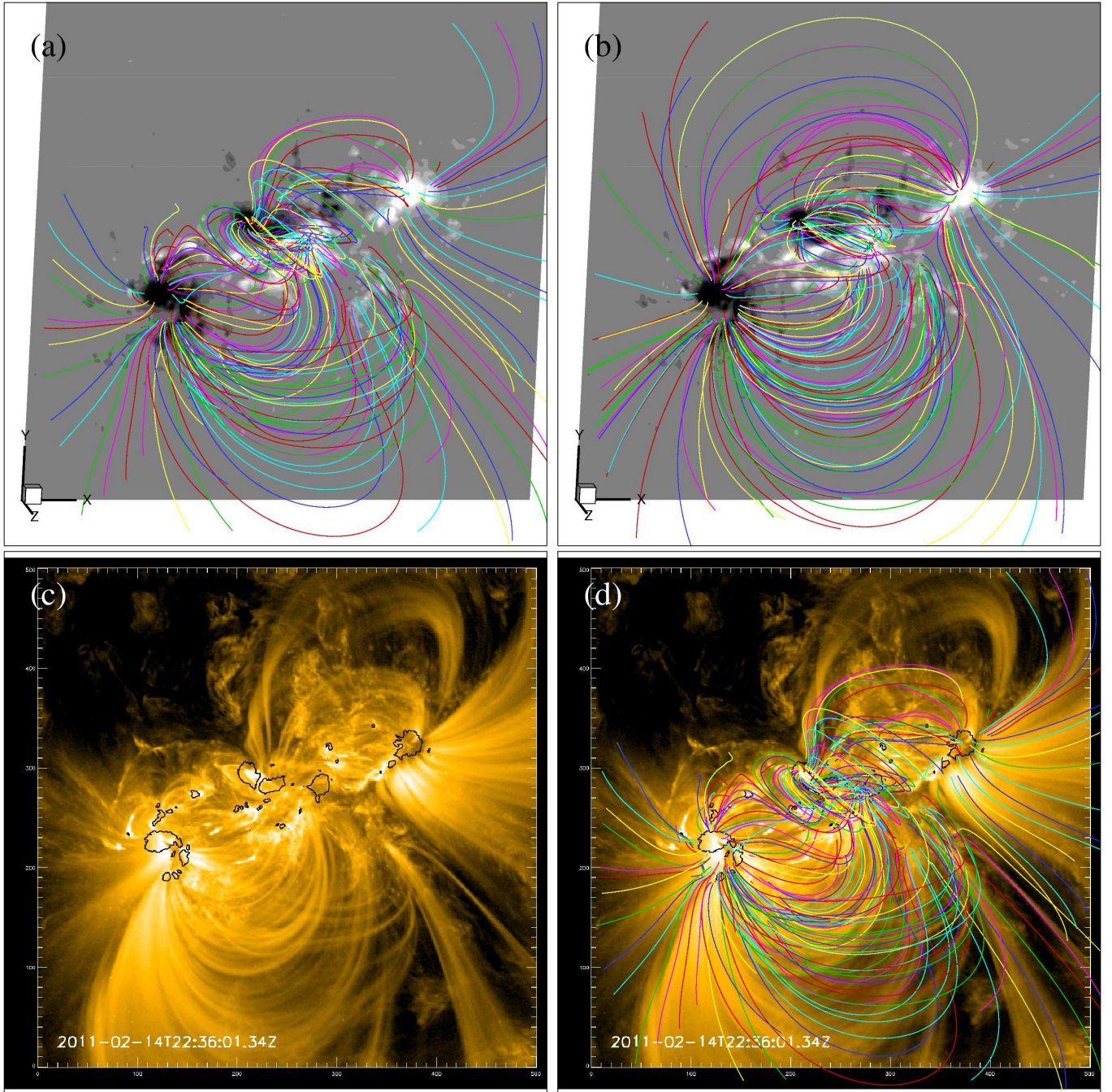


FIG. 5.— Comparison of extrapolation field lines with AIA 171 Å loops for AR 11158: the NLFFF lines (a), the potential field lines (b), the AIA image (c) and NLFFF lines overlaying the AIA image (d). Contour lines for ± 1000 G (the black curves) of LoS photospheric field are over-plotted on the AIA images, and for all the panels the field lines are traced from the same set of footpoints on the bottom surface.

ergy E_{free}

$$E_{\text{tot}} = \int_V \frac{B^2}{8\pi} dV, \quad E_{\text{pot}} = \int_V \frac{B_{\text{pot}}^2}{8\pi} dV, \quad E_{\text{free}} = E_{\text{tot}} - E_{\text{pot}} \quad (11)$$

where B_{pot} is the potential field strength. Results of the metrics are given in Table 2 for extrapolations from both the raw and preprocessed magnetograms. We compute the metrics for four different regions including the full extrapolation box and the subregions A, B, and C as outlined in Figure 6.

For the full region, our results of the current-weighted sine is ~ 0.3 , which means the mean misalignment angle between the magnetic field and current is about 17° . Such value is much larger than those from our previous benchmark tests using ideal or synthetic magnetograms (which are ~ 0.1 (6°) or smaller, see Jiang & Feng 2012a), but is comparable to previously reported results by other NLFFF codes on real magnetograms (e.g., the average CWsin by various NLFFF codes applied to AR 10930 (Schrijver et al. 2008) and AR 10953 (DeRosa et al. 2009) are 0.36 and 0.28, respectively). With such a large mis-

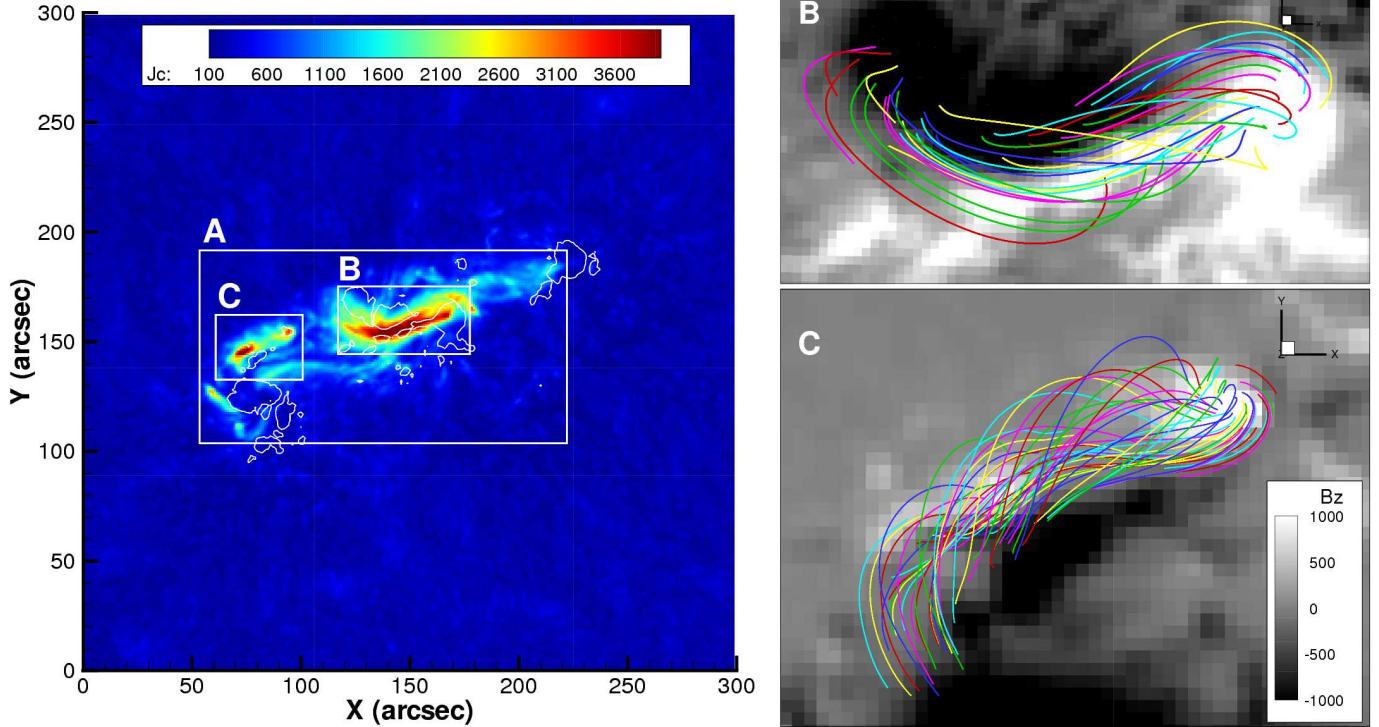


FIG. 6.— Strong-current regions and their magnetic structures for AR 11158. Left panel is image of the vertical integral of current density, i.e., $J_C = \int |\mathbf{J}| dz$ where the current is calculated by $\mathbf{J} = \nabla \times \mathbf{B}$ with a unit of G pixel^{-1} ; Regions of strong current are outlined by the boxes A, B and C. Right panels show the magnetic structures of the strong-current regions of B and C.

alignment angle, the result seems to be far away from an exactly force-free solution which has a zero misalignment angle. However it should be noted that the metric CW_{sin} may not be a good monitor for numerical solutions, which unavoidably have random numerical errors because of limited resolution. As a simple example, CW_{sin} is close to 1 even for a potential field solution computed by Green's function method or other numerical realization. The reason is that the numerical difference, used for computing the current $\mathbf{J} = \nabla \times \mathbf{B}$ from \mathbf{B} , gives small but finite currents, whose directions are randomly from 0° to 180° , thus an average of the full volume should give a misalignment angle of $\sim 90^\circ$. The noise in the observation data, mainly in the weak field regions, is also a major source for the random numerical errors. In these regions, the actual magnetic elements are probably smaller than the observed or numerical pixel size, and the field directions generally exhibit a random pattern on the image. To reduce such errors in computing the metric, we can either put larger weight of current (e.g., use C^2W_{sin}) or compute CW_{sin} within the strong-current subregions only. As is expected, the misalignment angle decreases significantly by measuring in this way. For the full region, C^2W_{sin} are only half of CW_{sin} . For the subregions, CW_{sin} are also only half or less for the full region, reaching the level of those from the benchmark tests (Jiang & Feng 2012a). In particular, the misalignment angle is only about 4° in subregion B, showing that the force-free assumption is modeled very well.

Regarding the energy contents, it is interesting to note that the free energy of subregion A exceeds that of the full region, meaning that the free energy content in the full volume excluding subregion A is negative. This is,

however, not surprising as we know that any sub-volume energy content of the non-potential field may be lower than the potential energy (e.g., Mackay et al. 2011; Jiang et al. 2012a). Also the measurement error may result in this negative free energy since it is very small compared to the total free energy. No matter which case is true, it can be clearly seen that the spatial distribution of free energy is largely co-spatial with that of the current, since the subregion A contains most of the currents of the whole volume. This confirms that the free energy in the corona is actually stored by the current-carrying field (where non-potentiality is strong), but not necessarily in the magnetic flux concentrations.

Finally, we compare the results extrapolated from the raw and preprocessed magnetograms. Inspecting of the force-freeness and divergence-freeness metrics shows that the improvement by preprocessing is negligible. This is because the raw data already satisfies the boundary force-free conditions well. Due to the smoothing, the result for the preprocessed data gives slightly lower energy contents than those for the raw data.

4.2. AR 11283

Figure 7 compares the AIA 171 \AA loops with the reconstructed field in the same way as Figure 5. For this AR, the NLFFF model appears to perform only slightly better than the potential model (there are some loops even worse produced by the NLFFF model than the potential model near the north-east boundary of the FoV). The clearest misalignment with the observation is the large closed loop pointed by the arrow in AIA image. This group of loops are failed to be recovered by both the potential and force-free models which give open field

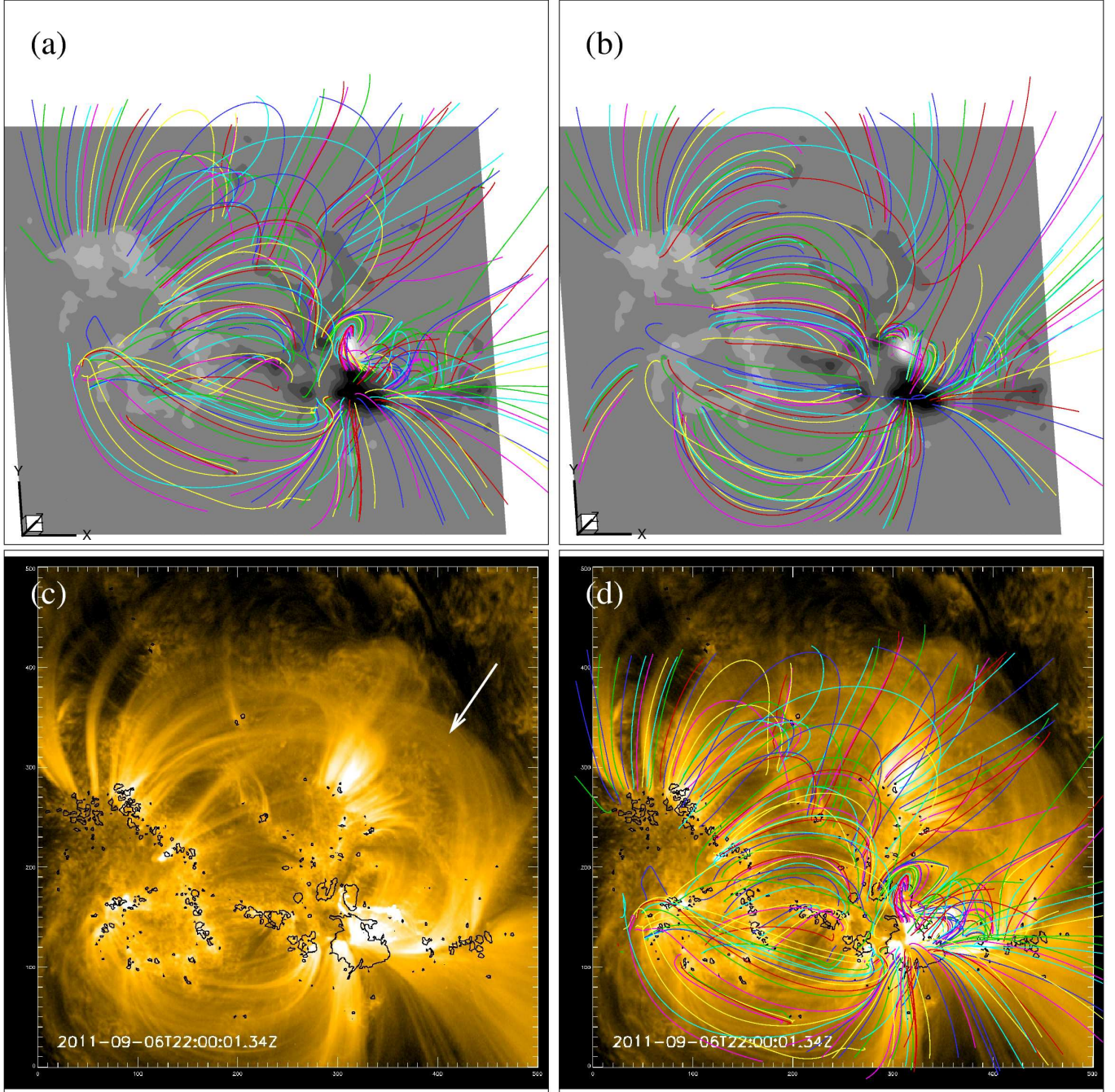


FIG. 7.— Same as Figure 5 but for AR 11283.

| Region | CWsin | C ² Wsin | $\langle f_i \rangle$ | E_{tot} | E_{pot} | E_{free} | $E_{\text{free}}/E_{\text{pot}}$ | $E_{\text{free}}/(E_{\text{free}})_{\text{full}}$ |
|--------------|-------|---------------------|-------------------------|------------------|------------------|-------------------|----------------------------------|---|
| Raw | | | | | | | | |
| Full | 0.40 | 0.24 | 9.65E-04 | 5.94 | 5.58 | 0.46 | 8% | 100% |
| A | 0.15 | 0.09 | 3.69E-03 | 1.86 | 1.33 | 0.53 | 40% | 115% |
| Preprocessed | | | | | | | | |
| Full | 0.32 | 0.18 | 8.28E-04 | 6.10 | 5.12 | 0.98 | 19% | 100% |
| A | 0.13 | 0.09 | 1.76E-03 | 2.05 | 1.18 | 0.87 | 74% | 89% |

TABLE 3

RESULTS OF THE METRICS FOR AR 11283. FULL REGION IS EXTRAPOLATION BOX OF $[0, 300](x) \times [0, 256](y) \times [0, 150](z)$. REGION A IS $[193, 251] \times [86, 140] \times [0, 30]$. THE FOVS OF THE REGIONS ARE SHOWN BY THE BOX IN FIGURE 8. THE ENERGY UNIT IS 10^{32} ERG.

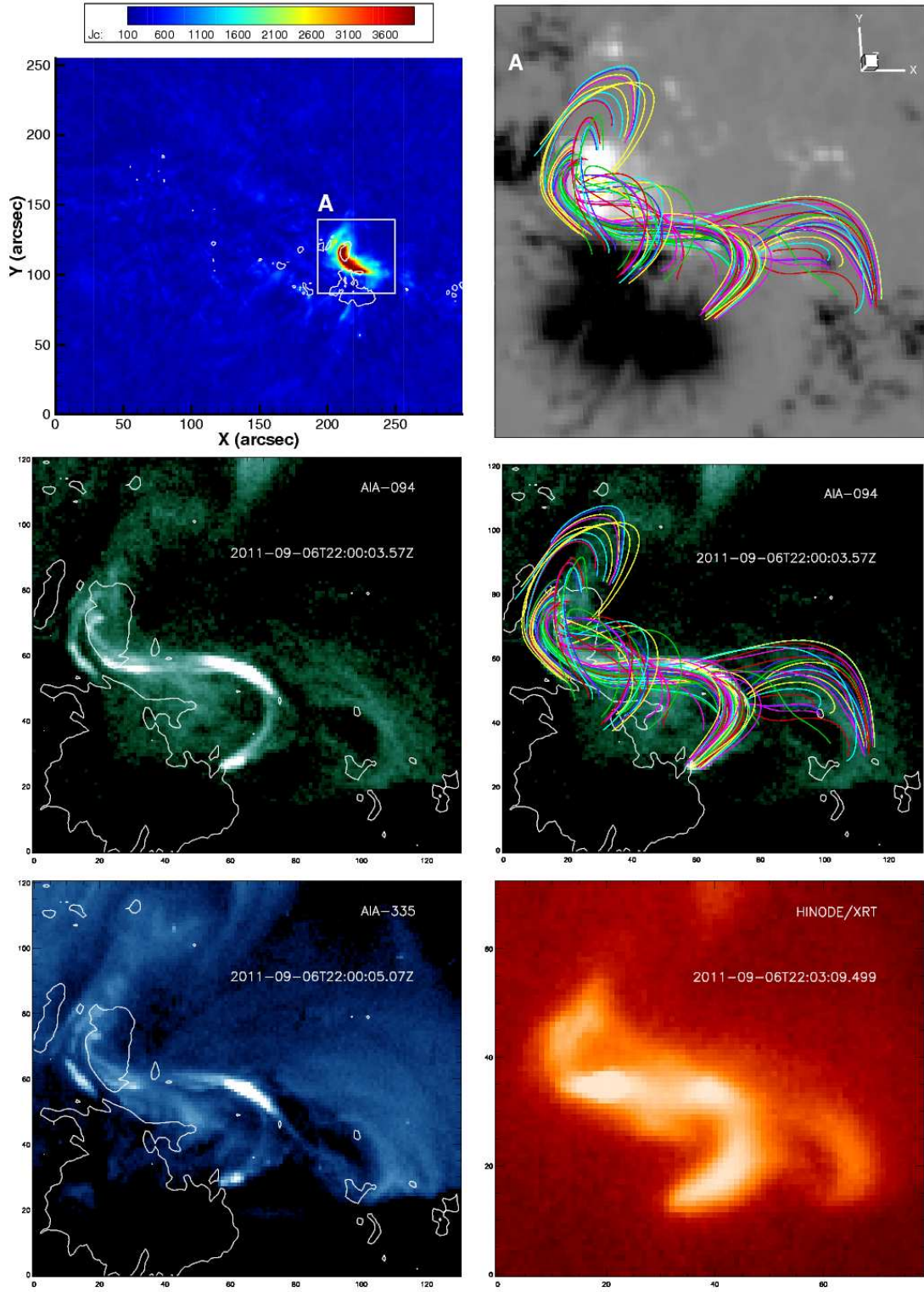


FIG. 8.— Strong-current region and its magnetic structure for AR 11283. The upper-left panel is image of the vertical integral of current density, i.e., $J_C = \int |\mathbf{J}| dz$; and upper-right panel shows the magnetic structure of subregion A, where a sigmoid, shown in the following panels, is observed clearly by *SDO/AIA* and *Hinode/XRT*.

lines instead. This, however, is not unexpected since the inputted magnetogram has flux unbalanced by -10% . So there must be field lines from the negative polarity opening in the FoV. The reason for this flux unbalance may be that the positive flux in the east is rather dispersed (much more than the negative polarity), and thus properly be underestimated by the observation.

Near the major polarity the structure of the loops is very complex and the extrapolated field shows highly sheared and twisted structures, indicating a significant non-potentiality there. Actually this was the site of the flare and filament eruption. The distribution of the vertically integrated current shows a strong concentration of current in this region, as denoted by A in Figure 8. In the same figure, we show the local field structure and the observations from different wavelengths of much higher temperature than 171 Å. The magnetic field exhibits a multi-flux rope configuration. The most remarkable structure is a sigmoid, i.e., the S-shaped loop in the AIA 94 Å and 335 Å images. The sigmoid can be seen most clearly in the AIA 94 Å wavelength (6.3 MK) with rather thin but enhanced shape, and is also well shaped in the soft X-ray image taken by *Hinode*/XRT. In the fourth panel of the figure the field lines are plotted overlying on the AIA 94 Å image. It demonstrates that our extrapolation has recovered the sigmoid rather precisely, at least in morphology (see the precise alignment of the field lines with the shape of the sigmoid). The distribution of the current also resembles roughly the shape of the sigmoid, suggesting that the enhancement of EUV and X-ray emission associated with the sigmoid is made by the strong field-aligned current via Joule heating of the plasma. This sigmoid locates between the major positive and negative polarities and the currents reside mostly in the north-east part, as shown by the current distribution. The twist of the sigmoid field lines is not strong as modeled in other cases such as Rousev et al. (2012) or Savcheva et al. (2012), and this sigmoid is composed of a single flux rope, which is also different from their results with two flux ropes or double-J shaped current pattern. The observation and modeling suggest that there seems to be another flux rope overlying the sigmoid, and the flare and CME may be resulted by the eruptions of these flux ropes, which is left for future study.

Similarly, we compute the metrics of force-freeness and divergence-freeness for both the full region and the sub-region and the results are given in Table 3. By comparing the results using the raw and preprocessed data, we find that evidently the preprocessed result is closer to force free, especially of the full region for which the raw data gives $CW_{\text{sin}} \sim 0.4$ (24°) while the preprocessed data gives $CW_{\text{sin}} \sim 0.3$ (17°). Thus for this AR the preprocessing indeed improves the extrapolation greatly. Also the divergence is reduced by the preprocessing. It is noticeable that the total energy content is doubled by the preprocessing, reaching 10^{32} erg. But even this improvement of the free energy is likely to underestimate the actual value, considering that a X-class flare and CME erupted immediately (Feng et al. 2013). Still the current is strongly localized and the free energy is concentrated within the strong-current region, i.e., subregion A, which occupies only less than one percent of the full volume, but contains most of the free energy.

4.3. Convergence Study

It is important to monitor the relaxation process to study whether the iteration converges, since there is no theory to guarantee this. Here we study the convergence process of the computations by temporal evolution of several monitors, including the residual of field between two successive iterations

$$\text{res}^n(\mathbf{B}) = \sqrt{\frac{1}{3} \sum_{\delta=x,y,z} \frac{\sum_i (B_{i\delta}^n - B_{i\delta}^{n-1})^2}{\sum_i (B_{i\delta}^n)^2}} \quad (12)$$

(where n denotes the iteration step), the metric CW_{sin} and the total energy content. We record the residual by every ten steps and compute CW_{sin} and total energy by every ten τ_A . Results for extrapolation of both ARs are plotted in Figure 9. As can be seen, the system converges smoothly and fast. During the first 10 τ_A , the residual keeps increasing because the transverse field is inputted at the bottom continuously, which drives the system away from the initial potential field. After this driving process, the residual drops immediately, indicating a fast relaxation of the system. With about 40 τ_A (nearly 10000 iterations), the residual is already reduced to $\sim 10^{-5}$, and all the metrics and energy almost stagnate afterward. Thus the computations can actually be terminated once the residual is below 10^{-5} , which is consistent with our previous studies for benchmark cases (Jiang & Feng 2012a; Jiang et al. 2012b). It is also noteworthy that the convergence process is rather smooth, without any obvious oscillation or abrupt variation of the residual or the metrics, so the iteration is “safe”. This is a good feature of our code over other iteration codes for extrapolation, e.g., the Valori et al. (2007)’s magnetofrictional code or the Wheatland (2006)’s Grad-Rubin-like code, which usually show strong oscillatory in the iteration or even fail to converge occasionally (Schrijver et al. 2008; DeRosa et al. 2009).

5. CONCLUSIONS

In this paper we have applied the CESE-MHD-NLFFF code to the *SDO*/HMI vector magnetograms. Two ARs are sampled for the test, AR 11158 and AR 11283, both of which produced X-class flares and were very non-potential. We compared the results with the *SDO*/AIA images, showing that the reconstructed field lines resemble well most of the plasma loops, which is a basic requirement for an applicable NLFFF modeling code (DeRosa et al. 2009). Because the magnetic flux of the AR 11283 magnetogram is not well balanced, the extrapolation of the large scale field appears not as good as that for AR 11158. Observation shows that in the core regions of the ARs there were filament or sigmoid which are important precursors of eruptions like flares and CMEs. We also found in these places, there were highly-sheared and twisted field lines, i.e., flux ropes, which contain strong field-aligned currents and plenty of non-potential energy, and our extrapolations recovered indeed well those observed features, especially the sigmoid in AR 11283. By computing the metric CW_{sin} which measures mean value of misalignment between the magnetic field and electric current, we found that, the force-free constraint is fulfilled very well in the strong-field regions ($CW_{\text{sin}} \approx 0.1$, misalignment about 6°) but

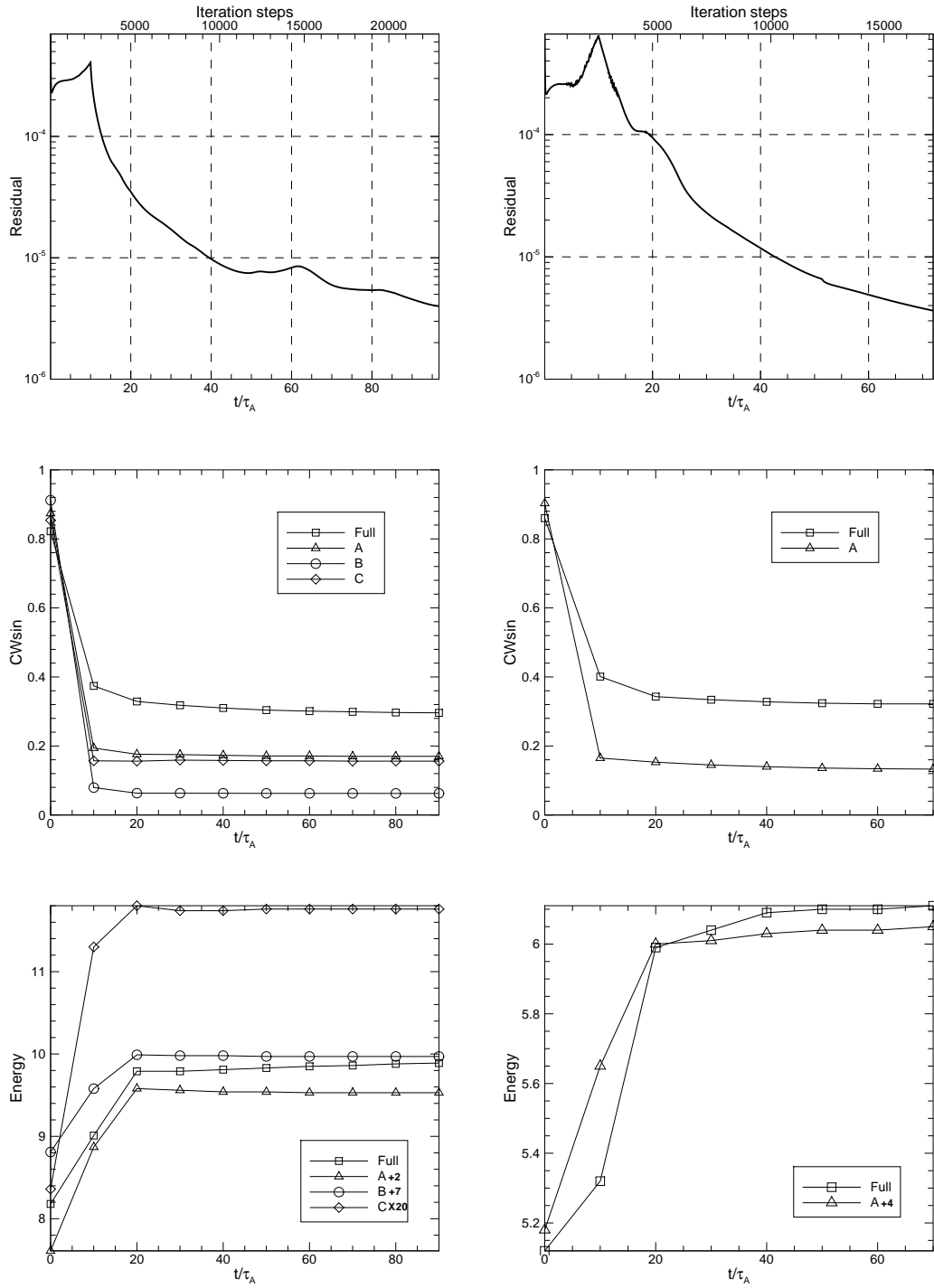


FIG. 9.— Convergence of computations: temporal evolution of the residual, the metric CWsin and the total energy content in the iteration process for AR 11158 (left column) and AR 11283 (right column). Note that for a better plot for the energy contents of different regions, their values are scaled properly as shown in the line legends.

apparently not that well in the weak-field regions ($CW_{\text{sin}} \approx 0.3$, misalignment about 17°) because of the data noise and the numerical errors of the small currents. The energy contents of our results are also consistent with the previous computations (with respect to the AR 11158, e.g., [Wiegelmann et al. 2012](#); [Sun et al. 2012b](#)). In summary our extrapolation code can be used as a viable tool to study the 3D magnetic field in the corona.

We developed the CESE-MHD-NLFFF code not only for field extrapolation, but also as a sub-program for the project of data-driven MHD modeling of the ARs, the eruptions and their dynamic evolutions in the global corona using continuously-observed data on the photosphere. At present numerical MHD investigations of the solar eruptions ([Amari et al. 2003](#); [MacNeice et al. 2004](#); [Aulanier et al. 2009](#); [Fan 2010](#); [Török et al. 2011](#); [Roussev et al. 2012](#)) are mostly based on idealized magnetic configurations without constrained by real observations. A step forward of understanding what really happens in the solar eruptions, certainly necessitates the observation-constrained numerical model. For example, considering that NLFFF extrapolation can recover highly-sheared magnetic arches and twisted flux ropes, which are basic building blocks of many eruption models (e.g., [Török &](#)

[Kliem 2005](#); [Aulanier et al. 2009](#)), utilizing the extrapolated field from real magnetograms can obviously provide much more realistic initial inputs than those idealized models like [Titov & Démoulin \(1999\)](#)'s flux rope model. Our future work is to input the extrapolation field as an initial condition into the data-driven full MHD model ([Jiang et al. 2012a](#); [Feng et al. 2012](#)), along with the surface plasma flows derived from time-series of photosphere magnetograms (e.g., [Liu et al. 2012](#)) as bottom boundary condition to stress the model, with an objective to better simulate the initiation and evolution of solar explosive phenomena and their interplanetary evolution process.

This work is jointly supported by the 973 program under grant 2012CB825601, the Chinese Academy of Sciences (KZZD-EW-01-4), the National Natural Science Foundation of China (41204126, 41274192, 41031066, and 41074122), and the Specialized Research Fund for State Key Laboratories. Data are courtesy of NASA/SDO and the HMI science teams. C. W. Jiang thanks Dr. X. Luo for a careful revise of the text. The authors thank the anonymous referee for invaluable comments.

REFERENCES

- Aly, J. J. 1989, *Sol. Phys.*, 120, 19
 Amari, T., Aly, J. J., Luciani, J. F., Boulmezaoud, T. Z., & Mikic, Z. 1997, *Sol. Phys.*, 174, 129
 Amari, T., Boulmezaoud, T. Z., & Mikic, Z. 1999, *A&A*, 350, 1051
 Amari, T., Luciani, J. F., Aly, J. J., Mikic, Z., & Linker, J. 2003, *ApJ*, 585, 1073
 Aschwanden, M. J. 2011, *Living Reviews in Solar Physics*, 8, 5
 Aschwanden, M. J., Wuelsel, J.-P., Nitta, N. V., Lemen, J. R., DeRosa, M. L., & Malanushenko, A. 2012, *ApJ*, 756, 124
 Aulanier, G., Török, T., Démoulin, P., & DeLuca, E. E. 2009, *ApJ*, 708, 314
 Borrero, J., Tomczyk, S., Kubo, M., Socas-Navarro, H., Schou, J., Couvidat, S., & Bogart, R. 2011, *Solar Physics*, 273, 267
 DeRosa, M. L., Schrijver, C. J., Barnes, G., Leka, K. D., Lites, B. W., Aschwanden, M. J., Amari, T., Canou, A., McTiernan, J. M., Régnier, S., Thalmann, J. K., Valori, G., Wheatland, M. S., Wiegelmann, T., Cheung, M. C. M., Conlon, P. A., Fuhrmann, M., Inhester, B., & Tadesse, T. 2009, *ApJ*, 696, 1780
 Fan, Y. 2010, *ApJ*, 719, 728
 Feng, L., Wiegelmann, T., Su, Y., Inhester, B., Li, Y. P., Sun, X. D., & Gan, W. Q. 2013, *ApJ*, 765, 37
 Feng, X., Jiang, C., Xiang, C., Zhao, X., & Wu, S. 2012, *The Astrophysical Journal*, 758, 62
 Feng, X., Yang, L., Xiang, C., Jiang, C., Ma, X., Wu, S. T., Zhong, D., & Zhou, Y. 2012, *Sol. Phys.*, 279, 207
 Inoue, S., Kusano, K., Magara, T., Shiota, D., & Yamamoto, T. T. 2011, *ApJ*, 738, 161
 Jiang, C. W., Feng, X., Fan, Y., & Xiang, C. 2011, *ApJ*, 727, 101
 Jiang, C. W., Feng, X., Wu, S. T., & Hu, Q. 2012a, *ApJ*, 759, 85
 Jiang, C. W., Feng, X., & Xiang, C. 2012b, *ApJ*, 755, 62
 Jiang, C. W. & Feng, X. S. 2012a, *ApJ*, 749, 135
 Jiang, C. W. & Feng, X. S. 2013, *Sol. Phys.*, Under review
 Jiang, C. W., Feng, X. S., Zhang, J., & Zhong, D. K. 2010, *Sol. Phys.*, 267, 463
 Jing, J., Park, S.-H., Liu, C., Lee, J., Wiegelmann, T., Xu, Y., Deng, N., & Wang, H. 2012, *ApJ*, 752, L9
 Leka, K., Barnes, G., Crouch, A., Metcalf, T., Gary, G., Jing, J., & Liu, Y. 2009, *Solar Physics*, 260, 83
 Liu, Y., Zhao, J., & Schuck, P. W. 2012, *Sol. Phys.*, 195
 Low, B. C. & Lou, Y. Q. 1990, *ApJ*, 352, 343
 Mackay, D. H., Green, L. M., & van Ballegooijen, A. 2011, *ApJ*, 729, 97
 MacNeice, P., Antiochos, S. K., Phillips, A., Spicer, D. S., DeVore, C. R., & Olson, K. 2004, *ApJ*, 614, 1028
 Malanushenko, A., Schrijver, C. J., DeRosa, M. L., Wheatland, M. S., & Gilchrist, S. A. 2012, *ApJ*, 756, 153
 McClymont, A. N., Jiao, L., & Mikic, Z. 1997, *Sol. Phys.*, 174, 191
 Metcalf, T. R., DeRosa, M. L., Schrijver, C. J., Barnes, G., van Ballegooijen, A. A., Wiegelmann, T., Wheatland, M. S., Valori, G., & McTiernan, J. M. 2008, *Sol. Phys.*, 247, 269
 Metcalf, T. R., Jiao, L., McClymont, A. N., Canfield, R. C., & Uitenbroek, H. 1995, *ApJ*, 439, 474
 Molodenskii, M. M. 1969, *Soviet Ast.*, 12, 585
 Roumeliotis, G. 1996, *ApJ*, 473, 1095
 Roussev, I., Galsgaard, K., Downs, C., Lugaz, N., Sokolov, I., Moise, E., & Lin, J. 2012, *Nature Physics*, 8, 845
 Sakurai, T. 1989, *Space Sci. Rev.*, 51, 11
 Savcheva, A. S., van Ballegooijen, A. A., & DeLuca, E. E. 2012, *ApJ*, 744, 78
 Schrijver, C. J., Aulanier, G., Title, A. M., Pariat, E., & Delannée, C. 2011, *ApJ*, 738, 167
 Schrijver, C. J., De Rosa, M. L., Metcalf, T. R., Liu, Y., McTiernan, J., Régnier, S., Valori, G., Wheatland, M. S., & Wiegelmann, T. 2006, *Sol. Phys.*, 235, 161
 Schrijver, C. J., DeRosa, M. L., Metcalf, T., Barnes, G., Lites, B., Tarbell, T., McTiernan, J., Valori, G., Wiegelmann, T., Wheatland, M. S., Amari, T., Aulanier, G., Démoulin, P., Fuhrmann, M., Kusano, K., Régnier, S., & Thalmann, J. K. 2008, *ApJ*, 675, 1637
 Sun, X., Hoeksema, J. T., Liu, Y., Chen, Q., & Hayashi, K. 2012a, *ApJ*, 757, 149
 Sun, X., Hoeksema, J. T., Liu, Y., Wiegelmann, T., Hayashi, K., Chen, Q., & Thalmann, J. 2012b, *ApJ*, 748, 77
 Titov, V. S. & Démoulin, P. 1999, *A&A*, 351, 707
 Török, T. & Kliem, B. 2005, *ApJ*, 630, L97
 Török, T., Panasenco, O., Titov, V. S., Mikić, Z., Reeves, K. K., Velli, M., Linker, J. A., & De Toma, G. 2011, *ApJ*, 739, L63
 Turmon, M., Jones, H. P., Malanushenko, O. V., & Pap, J. M. 2010, *Sol. Phys.*, 262, 277
 Valori, G., Kliem, B., & Fuhrmann, M. 2007, *Sol. Phys.*, 245, 263
 Wheatland, M. S. 2006, *Sol. Phys.*, 238, 29
 Wheatland, M. S., Sturrock, P. A., & Roumeliotis, G. 2000, *ApJ*, 540, 1150
 Wiegelmann, T. 2004, *Sol. Phys.*, 219, 87
 —. 2008, *J. Geophys. Res.*, 113, 3
 Wiegelmann, T., Inhester, B., & Sakurai, T. 2006, *Sol. Phys.*, 233, 215
 Wiegelmann, T. & Sakurai, T. 2012, *Living Rev. Solar Phys.*, 9
 Wiegelmann, T., Thalmann, J. K., Inhester, B., Tadesse, T., Sun, X., & Hoeksema, J. T. 2012, *Sol. Phys.*, 67
 Wu, S. T., Sun, M. T., Chang, H. M., Hagyard, M. J., & Gary, G. A. 1990, *ApJ*, 362, 698
 Yan, Y. & Sakurai, T. 2000, *Sol. Phys.*, 195, 89
 Yang, L. P., Feng, X. S., Xiang, C. Q., Liu, Y., Zhao, X., & Wu, S. T. 2012, *Journal of Geophysical Research (Space Physics)*, 117, 8110